Electronic Supplementary Material (ESI) for Nanoscale.
This journal is © The Royal Society of Chemistry 2022

Supporting Information:
Revealing the impact of strain in the optical properties of bubbles in monolayer $MoSe_2$

F. S. Covre[a], P. E. Faria Junior[b], V. O. Gordo[c], C. Serati de Brito[a], Y. V. Zhumagulov[b], M. D. Teodoro[a], O. D. D. Couto Jr.[c], L. Misoguti[d], S. Pratavieira[d], M. B. Andrade[d], P. C. M. Christianen[e], J. Fabian[b], F. Withers[f], and Y. Galvão Gobato*[a]

[a]Departamento de Física, Universidade Federal de São Carlos, 13565-905, São Carlos, SP, Brazil
[b]Institute for Theoretical Physics, University of Regensburg, 93040 Regensburg, Germany
[c]Instituto de Física "Gleb Wataghin", Universidade Estadual de Campinas, 13083-859, Campinas, São Paulo, Brazil
[d]Instituto de Física de São Carlos- Universidade de São Paulo, CEP 13566-590, São Carlos, São Paulo, Brazil
[e]High Field Magnet Laboratory (HFML - EMFL), Radboud University, 6525 ED Nijmegen, The Netherlands
[f]College of Engineering, Mathematics and Physical Sciences, University of Exeter, Exeter EX4 4QF

1 Calculation of the exciton energy

The exciton properties of monolayer transition metal dichalcogenides (TMDCs) are calculated via the effective Bethe-Salpeter equation (BSE)[1–4] considering parabolic bands with the Rytova-Keldish (RK) potential[5–8] mediating the electron-hole electrostatic interaction, which accurately describes 2D monolayers subjected to different dielectric environments[8–18].

The BSE for excitons in k-space reads

$$\left[\left(\frac{\hbar^2}{2m_0}\right)\frac{k^2}{\mu}-\Omega_\lambda\right]F_\lambda(\vec{k})-\sum_{\vec{k}'}\mathrm{V_{RK}}(\vec{k}-\vec{k}')\,F_\lambda(\vec{k}')=0\,, \tag{1}$$

with Ω_λ and $F_\lambda(\vec{k})$ being the exciton binding energy and wavefunction for the λ-th state, respectively, and the exction reduced mass is written as $\mu^{-1}=m_c^{-1}+m_v^{-1}$, with $m_{c(v)}$ being the effective mass of the conduction (valence) band.

The RK potential reads

$$\mathrm{V_{RK}}(\vec{K})=\frac{1}{\Lambda}\frac{e^2}{2\varepsilon_0}\frac{1}{\varepsilon K+r_0K^2} \tag{2}$$

with r_0 being the screening length of the TMDC and ε being the effective dielectric constant due to the surroundings, given by $\varepsilon=(\varepsilon_t+\varepsilon_b)/2$, with $\varepsilon_{t(b)}$ indicating the dielectric constant of the top (bottom) region adjacent to the TMDC.

We take into account the renormalization of the screening length due to the dielectric surroundings via

$$r_0(\varepsilon_t,\varepsilon_b)=\frac{d\varepsilon_m}{2}\left(1-\frac{\varepsilon_t^2+\varepsilon_b^2}{2\varepsilon_m^2}\right) \tag{3}$$

*yara@df.ufscar.br

in which d is the effective thickness of the TMDC and ε_m is the dielectric constant of the TMDC monolayer[8,19].

The band gap renormalization of the monolayer TMDC due to the dielectric screening[9,12] can be incorporated as

$$E_g(\varepsilon_t,\varepsilon_b) = E_0 + \Sigma(\varepsilon_t,\varepsilon_b)\,, \tag{4}$$

with

$$\Sigma(\varepsilon_t,\varepsilon_b) = \frac{e^2}{4\pi\varepsilon_0}\frac{1}{\varepsilon_m d}\left[\frac{L_t+L_b}{\sqrt{L_tL_b}}\tanh^{-1}\left(\sqrt{L_tL_b}\right) - \ln\left(1-L_tL_b\right)\right], \tag{5}$$

in which $L_i = (\varepsilon_m-\varepsilon_i)\,/\,(\varepsilon_m+\varepsilon_i)$, $i=t,b$. Note that $E_g(1,1) = E_0+\Sigma(1,1)$ is the band gap of the bare monolayer TMDC.

The final exciton energy, associated to the absorption or photoluminescence peak, is then given by

$$E_{\mathrm{X}} = E_g(\varepsilon_t,\varepsilon_b) - \Omega_{\mathrm{X}}(\varepsilon_t,\varepsilon_b)\,, \tag{6}$$

in which X refers to the excitonic state we are interested in. Particularly to our analysis to calibrate the parameters for $MoSe_2$, we are interested in the 1s and 2s states of the A exciton.

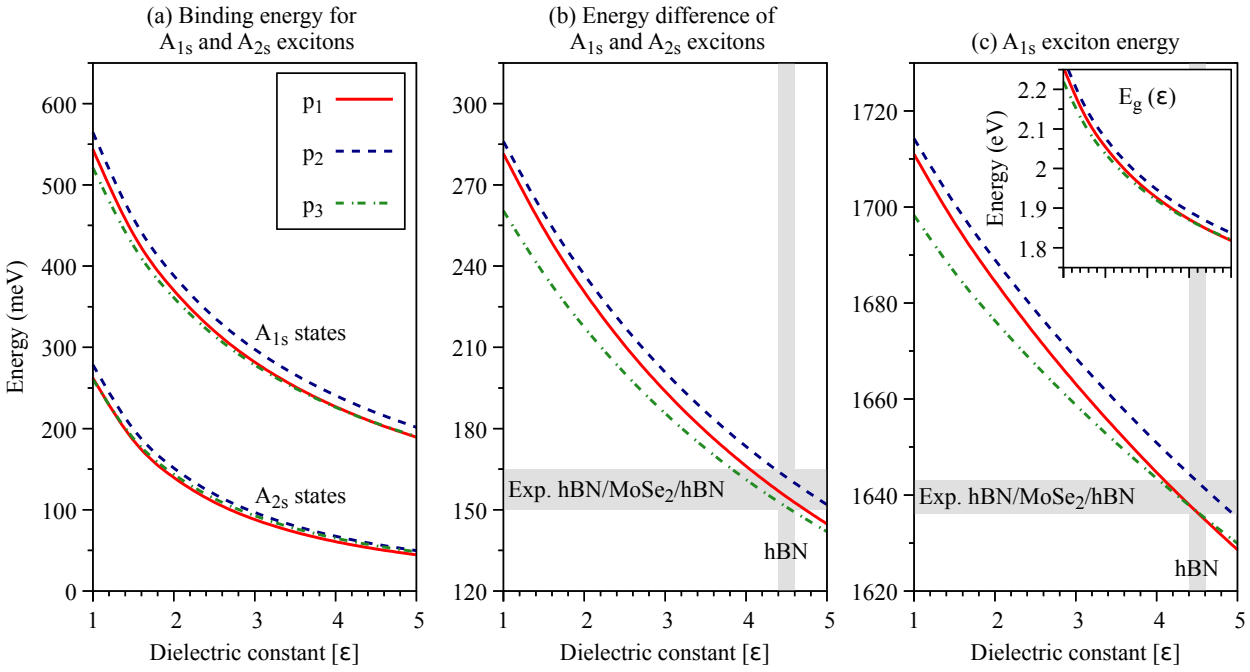

Figure S1: (a) Binding energies of 1s and 2s A excitons states, (b) energy difference between 1s and 2s A excitons binding energies and (c) the total 1s A exciton energy as function of the dielectric constant $\varepsilon = (\varepsilon_t+\varepsilon_b)/2$. The inset in panel (c) shows the band gap dependence with respect to ε, given by Eq. (4). The shaded regions in panels (b) and (c) represent the experimental data collected in Table S1. The parameter sets p_1-p_3 are given in Table S2.

The exciton energy E_{X} depends on the intrinsic parameters of the TMDC monolayer, namely, μ, r_0, d and E_0. To obtain a reliable parameters' set that captures the experimental values and allows us to understand the changes in the dielectric environment of the $MoSe_2$ bubble, we average different parameters available in the literature, summarized in Table S1. The energy variation of ~ 10 meV among the different experiments is consistent with typical dielectric disorder present in monolayer TMDCs[12]. Furthermore, it is also worth mentioning that the reduced exciton mass is not influenced by the dielectric environment[20]. The experimental values of r_0 given in Table S1 are a bit smaller than what is predicted by theory, for instance, Ref.[8] reports $r_0 = 5.2$ nm and $d = 6.0$ Å, and Ref.[21] provides $r_0 = 5.6$ nm and $d = 6.5$ Å. Taking into account the fluctuations in the experimental and theoretical values, we suggest three different parameter sets that best reproduce

Table S1: Parameters extracted from experimental studies on hBN/$MoSe_2$/hBN samples.

	μ	ε	r_0 (nm)	E_A (meV)	Δ_{21} (meV)	T (K)
Han *et al.* [15]	0.28	4.5	4.5	1636.0	150.0	4
Goryca *et al.* [16]	0.35	4.4	3.9	1643.0	165.0	4
Goldstein *et al.* [17]	0.35	4.5	4.5	1643.6	152.4	4

Table S2: Calibrated parameter sets used in the exciton calculations. The value of $E_0 = 1615$ meV is kept the same in all cases.

	μ	r_0 (nm)	d (Å)
p_1	0.30	4.5	6.5
p_2	0.35	4.5	6.0
p_3	0.35	5.0	6.5

the high-quality experiments in hBN encapsulated $MoSe_2$. These values are given in Table S2 and the calculated results are summarized in Fig. S1. By performing the calculations with these 3 parameter sets we are able to nicely capture the dielectric dependence in an energy window of ~ 10 of meV, as expected in real samples due to the dielectric disorder of the surroundings[12], and thus reproducing the experimental values given in Table S1. Furthermore, in Fig. 1 of the main text we show that these parameter sets nicely describe the A exciton peaks obtained via photoluminescence at the PMMA/$MoSe_2$/hBN region at nominally zero strain and allows us to understand the variation of strain and dielectric surroundings in different regions of the sample.

2 First principles calculations

We performed the first principles calculations of the orbital angular momentum using the density functional theory (DFT) implemented in the WIEN2k package[22]. We used the Perdew-Burke-Ernzerhof (PBE) exchange-correlation functional[23], a Monkhorst-Pack k-grid of 15×15 and self-consistent convergence criteria of 10-6 e for the charge and 10-6 Ry for the energy. We considered a core–valence separation energy of -6 Ry, atomic spheres with orbital quantum numbers up to 10 and the plane-wave cutoff multiplied by the smallest atomic radii is set to 9. For the spin-orbit coupling effects, the core electrons are treated fully relativistically whereas valence electrons are treated via a second variational procedure[24], with the scalar-relativistic wave functions calculated in an energy window of -10 to 10 Ry. The chosen energy window thus provides more than a 1000 bands, which are crucial for a proper convergence of the angular momentum implementation, as shown in Ref.[25]. The angular momenta of the conduction and valence band states that give rise to the A exciton are calculated with the the state-of-the-art approach given in Refs.[25–28]. The resulting g-factor of the Zeeman shift at the K-valley for the relevant conduction and valence bands is then written as $g_{c(v)} = L_{c(v)} + 1$, with the value of 1 referring to the spin-up character of the bands involved (spin-conserving optical transition). The A exciton g-factor is then given by $g_A = 2(g_c - g_v)$ with the prefactor 2 taking into account the time-reversal relation between K and -K valleys. We considered the unstrained $MoSe_2$ monolayer with lattice parameters of $a_0 = 3.289$ Å and $d_0 = 3.335$ Å[29] and the biaxial strain is applied by compressing or stretching the lattice parameter, accompanied with the change in the thickness as given by from Ref[4]. For all cases we considered a vacuum spacing of 16 Å to avoid self-interaction.

3 Experiments

Figure S2 shows the color-code mapping of the PL intensity as a function of the position at 300K for the same positions indicated in Figure 1. We observed that there is a clear red shift in the bubble region which depends on the laser position. Similar behaviour was observed in Figure 1 at

4K. Fig. S2-(b) illustrates typical PL spectrum in the flat region and in the bubble region .

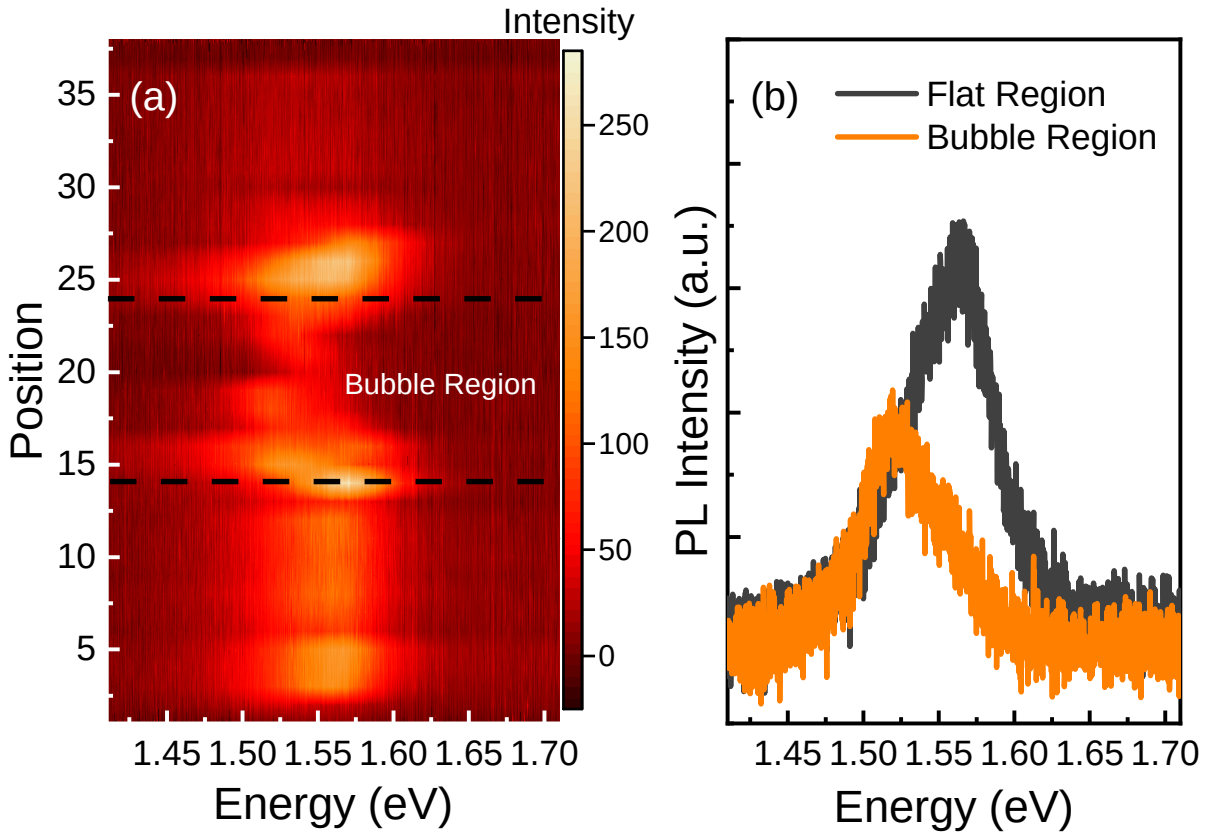

Figure S2: (a) Color-code mapping of the PL Intensity as a function of the position at 300K (b) Typical PL spectrum in the flat and bubble region also at 300K.

Figure S3 shows the E′ Raman mode for different laser positions on the sample measured with 633nm laser excitation at 300K. Figure S3-(b) shows the optical image of the sample and the laser positions of Raman measurements. We observe a clear blue shift on the edge of the bubble which indicates a compressive strain. On the other hand, a red shift of E´is observed in the bubble region. In addition, we remark that this red shift depends on the laser position in the bubble region. Similar behavior was observed for other Raman modes.

Figure S4-(a) shows typical PL spectra in the bubble region for 633nm laser excitation and 20 μW at 4K. Figure S4(b) shows the laser power dependence for L2 PL peak in low and high laser power regimes. In general, we have observed a non-linear laser power dependence probably due to a saturation of available trap sites in the ML $MoSe_2$. We have fitted the curves in different laser power regimes using the power law. It is well known that for a free exciton emission it is expected to observe a linear dependence with k=1. However, we have obtained lower values for k for both laser power regimes which indicates that the emission L2 is related to localized trap states in the bubble region.

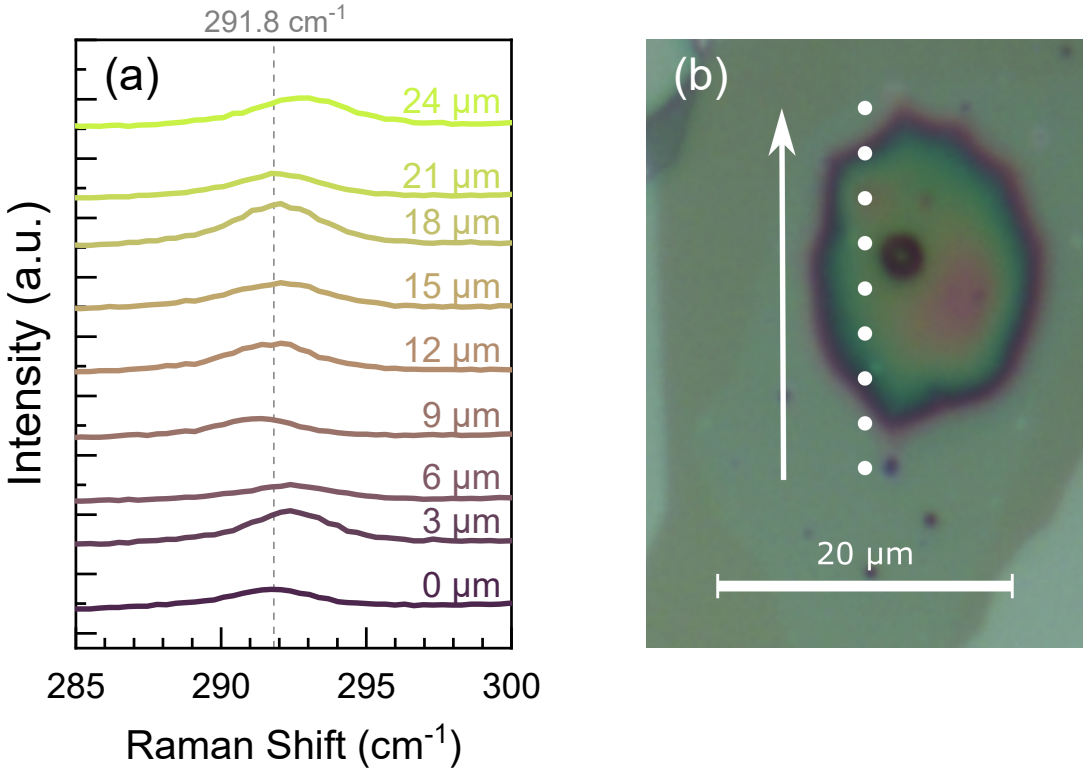

Figure S3: (a) Typical Raman spectra in the region of the E′ mode as a function of laser position measured with 633nm laser excitation at 300K (b) Optical image of the bubble and laser position of Raman measurements

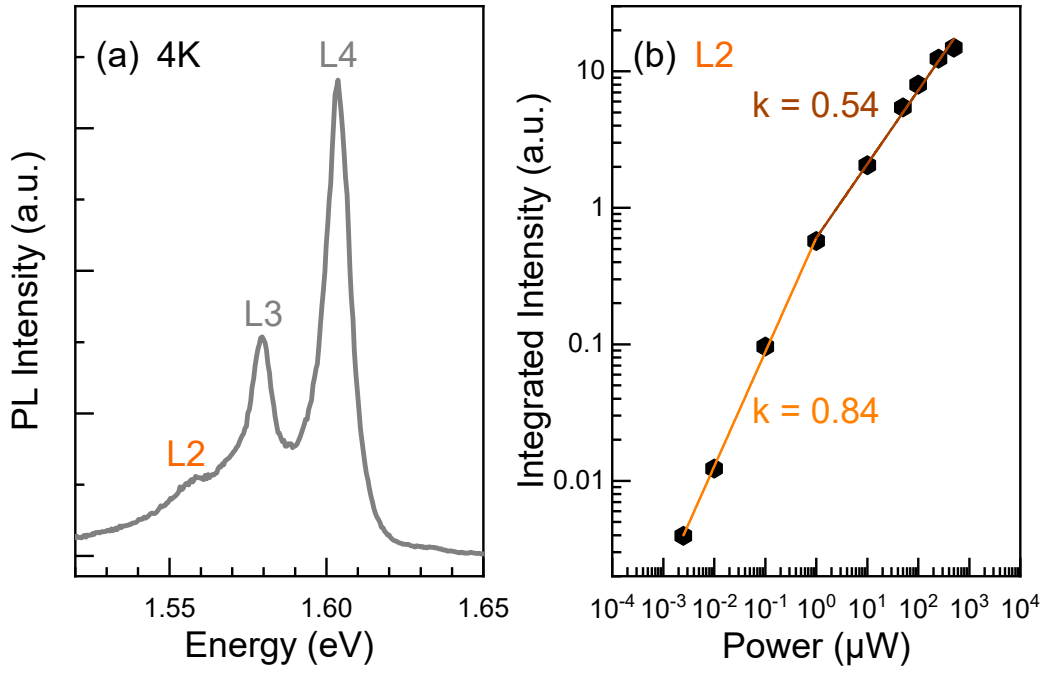

Figure S4: (a) PL spectrum in the bubble region and (b) Laser power dependence of L2 at 4K

Figure S5-shows the PL intensity as a function of time for the X and T emissions in the flat

region and for the L3 and L4 emissions in the bubble region at 4K. We have observed two decay components, the first being limited by our temporal resolution of our experimental setup. The PL decay times are shown in Figure S5-.In general, We have observed that X, T, L3 and L4 have similar PL decay times. We remark that the main component of the L4 and L3 emission has a very short lifetime. This result is consistent with the identification of L4 and L3 as exciton and trion respectively.

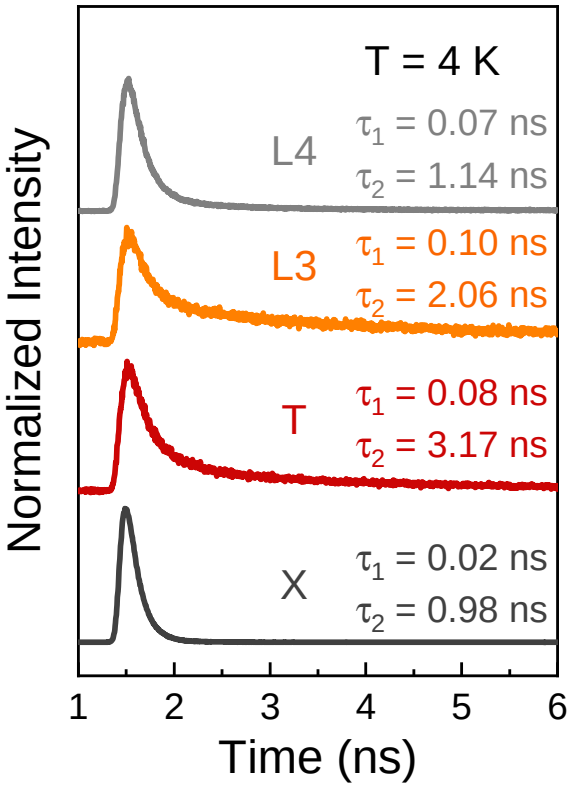

Figure S5: Time-resolved PL of X and T in the flat region and L3 and L4 in the bubble region at 4K. Two decay components are observed, the first being limited by the temporal resolution of our experimental system.

Figure S6-(a) shown the color code map of polarized the PL intensity as a function of magnetic field for a different position in the bubble region labelled A5. We have observed a complex behaviour for the PL peak energies as a function of magnetic field. Figure S6-(b) shows a typical polarization resolved PL at 0T and 6T. Figure S6-(c) shows the exciton splitting as function of magnetic field and the extracted exciton g-factor.

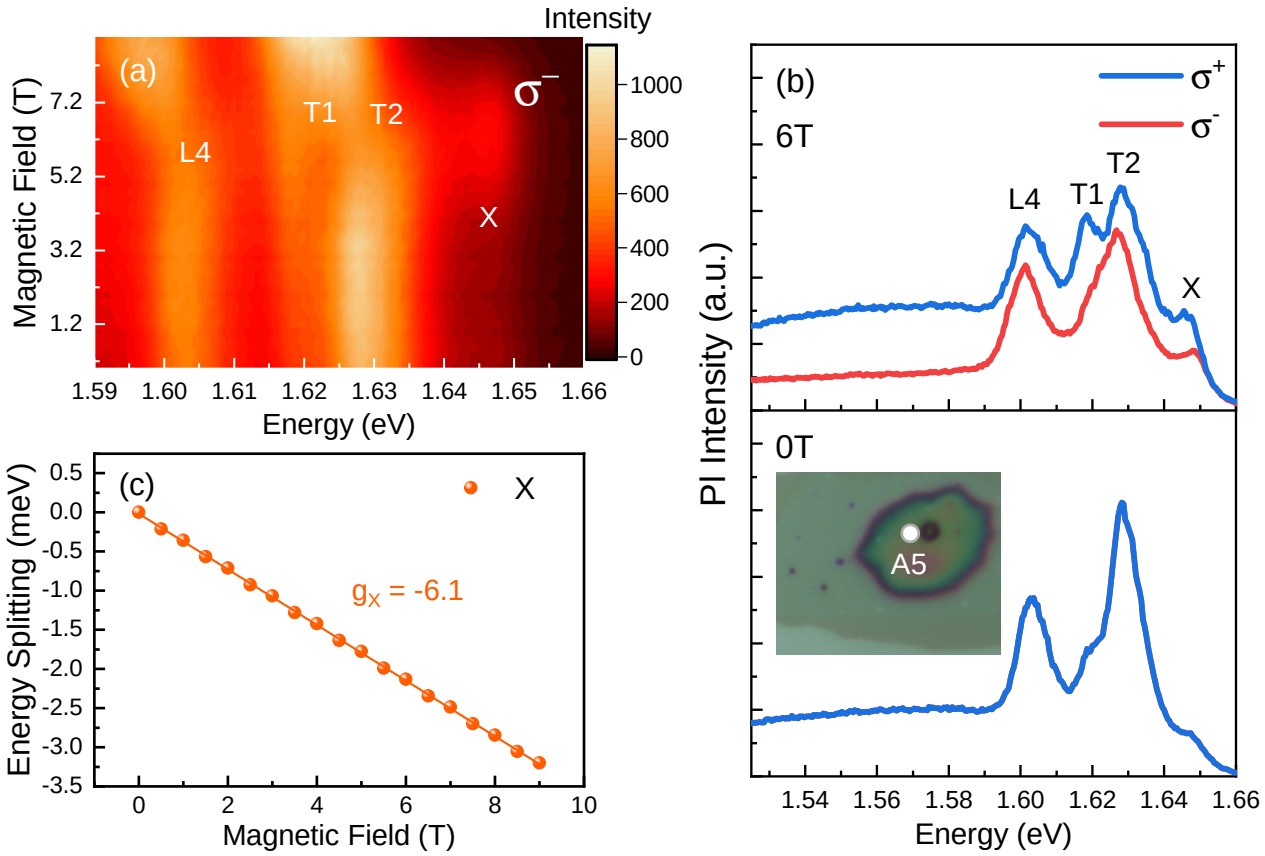

Figure S6: (a)Color code mapping of the μ-PL intensity versus magnetic field in the bubble region (position A5) under linearly polarized excitation.(b) Typical polarization resolved PL at 0T and 6T (c) Exciton energy splitting versus magnetic field at 4K

References

[1] M. Rohlfing and S. G. Louie, *Phys. Rev. Lett.*, 1998, **81**, 2312–2315.

[2] M. Rohlfing and S. G. Louie, *Phys. Rev. B*, 2000, **62**, 4927.

[3] P. E. Faria Junior, M. Kurpas, M. Gmitra and J. Fabian, *Phys. Rev. B*, 2019, **100**, 115203.

[4] K. Zollner, P. E. Faria Junior and J. Fabian, *Phys. Rev. B*, 2019, **100**, 195126.

[5] N. S. Rytova, *Mosc. Univ. Phys. Bull.*, 1967, **3**, 18.

[6] L. Keldysh, *Sov. J. Exp. Theo. Phys. Lett.*, 1979, **29**, 658.

[7] P. Cudazzo, I. V. Tokatly and A. Rubio, *Phys. Rev. B*, 2011, **84**, 085406.

[8] T. C. Berkelbach, M. S. Hybertsen and D. R. Reichman, *Phys. Rev. B*, 2013, **88**, 045318.

[9] Y. Cho and T. C. Berkelbach, *Phys. Rev. B*, 2018, **97**, 041409.

[10] A. Chernikov, T. C. Berkelbach, H. M. Hill, A. Rigosi, Y. Li, O. B. Aslan, D. R. Reichman, M. S. Hybertsen and T. F. Heinz, *Phys. Rev. Lett.*, 2014, **113**, 076802.

[11] A. Raja, A. Chaves, J. Yu, G. Arefe, H. M. Hill, A. F. Rigosi, T. C. Berkelbach, P. Nagler, C. Schüller, T. Korn *et al.*, *Nature communications*, 2017, **8**, 1–7.

[12] A. Raja, L. Waldecker, J. Zipfel, Y. Cho, S. Brem, J. D. Ziegler, M. Kulig, T. Taniguchi, K. Watanabe, E. Malic *et al.*, *Nature nanotechnology*, 2019, **14**, 832–837.

[13] A. V. Stier, K. M. McCreary, B. T. Jonker, J. Kono and S. A. Crooker, *Nature communications*, 2016, **7**, 1–8.

[14] A. V. Stier, N. P. Wilson, K. A. Velizhanin, J. Kono, X. Xu and S. A. Crooker, *Phys. Rev. Lett.*, 2018, **120**, 057405.

[15] B. Han, C. Robert, E. Courtade, M. Manca, S. Shree, T. Amand, P. Renucci, T. Taniguchi, K. Watanabe, X. Marie, L. E. Golub, M. M. Glazov and B. Urbaszek, *Phys. Rev. X*, 2018, **8**, 031073.

[16] M. Goryca, J. Li, A. V. Stier, T. Taniguchi, K. Watanabe, E. Courtade, S. Shree, C. Robert, B. Urbaszek, X. Marie *et al.*, *Nature communications*, 2019, **10**, 1–12.

[17] T. Goldstein, Y.-C. Wu, S.-Y. Chen, T. Taniguchi, K. Watanabe, K. Varga and J. Yan, *The Journal of Chemical Physics*, 2020, **153**, 071101.

[18] K.-Q. Lin, C. Shen Ong, S. Bange, P. E. Faria Junior, B. Peng, J. D. Ziegler, J. Zipfel, C. Bäuml, N. Paradiso, K. Watanabe *et al.*, *arXiv*, 2020, arXiv–2006.

[19] B. Scharf, D. Van Tuan, I. Žutić and H. Dery, *Journal of Physics: Condensed Matter*, 2019, **31**, 203001.

[20] L. Waldecker, A. Raja, M. Rösner, C. Steinke, A. Bostwick, R. J. Koch, C. Jozwiak, T. Taniguchi, K. Watanabe, E. Rotenberg, T. O. Wehling and T. F. Heinz, *Phys. Rev. Lett.*, 2019, **123**, 206403.

[21] A. Laturia, M. L. Van de Put and W. G. Vandenberghe, *npj 2D Materials and Applications*, 2018, **2**, 1–7.

[22] P. Blaha, K. Schwarz, F. Tran, R. Laskowski, G. K. Madsen and L. D. Marks, *The Journal of chemical physics*, 2020, **152**, 074101.

[23] J. P. Perdew, K. Burke and M. Ernzerhof, *Phys. Rev. Lett.*, 1996, **77**, 3865–3868.

[24] D. J. Singh and L. Nordstrom, *Planewaves, Pseudopotentials, and the LAPW method*, Springer Science & Business Media, 2006.

[25] T. Woźniak, P. E. Faria Junior, G. Seifert, A. Chaves and J. Kunstmann, *Phys. Rev. B*, 2020, **101**, 235408.

[26] T. Deilmann, P. Krüger and M. Rohlfing, *Phys. Rev. Lett.*, 2020, **124**, 226402.

[27] J. Förste, N. V. Tepliakov, S. Y. Kruchinin, J. Lindlau, V. Funk, M. Förg, K. Watanabe, T. Taniguchi, A. S. Baimuratov and A. Högele, *Nature Communications*, 2020, **11**, 4539.

[28] F. Xuan and S. Y. Quek, *Phys. Rev. Research*, 2020, **2**, 033256.

[29] A. Kormányos, G. Burkard, M. Gmitra, J. Fabian, V. Zólyomi, N. D. Drummond and V. Fal'ko, *2D Materials*, 2015, **2**, 022001.